

GESTRA: FIRST RESULTS OF LEO OBJECT PARAMETER ESTIMATION

N. Neuberger, S. Kollecker, M. Käske, S. Horstmann, and L. Prünke

Fraunhofer FHR, 53343 Wachtberg, Germany, Email: nadav.neuberger@fhr.fraunhofer.de

ABSTRACT

A sensitive detection of space debris within the Low Earth Orbit (LEO), and accurate estimation of their location, velocity and trajectory are crucial to increase near-earth safety and protecting billions of dollars' worth of space infrastructure. For this purpose, a Digital Array Radar (DAR) system has some unique abilities over the traditional optical technologies and common dish antennas. The newly-built semi-portable DAR system called the German Experimental Space Surveillance and Tracking Radar (GESTRA), is designed for the surveillance of space debris, orbiting at altitudes between 300 km and 3,000 km. We present initial successful experiments with an accurate parameter estimation of known space objects. With an orbit height of almost 900 km and 800 m/s of radial velocity, the estimation accuracy was below 100 m and a few m/s. The results are compared with propagated Two-Line Element (TLE) data and the system resolution limits. A complete description of the experiments along with detailed results is given.

Keywords: radar; space debris; SSA; LEO; phased-array.

1. INTRODUCTION

Earth's space infrastructure enables seamless operation of GNSS, internet, Earth Observation (EO), reconnaissance, weather forecasting satellites and much more. Most of it crosses the Low Earth Orbit (LEO) region in its orbit, which is sadly titled as the world's largest space waste belt, with millions of space debris [1].

One of the aspects of Space Situational Awareness (SSA) systems is to detect and track space debris, estimate its orbit trajectory and alert for potential collisions. They also provide the monitoring of life-threatening scenarios for the International Space Station (ISS) staff. For example, based on these predictions, in each year the ISS performs around four evasive manoeuvres, including entering escape capsules, to prepare for a potential hazardous collision [2].

Radar systems play an important role in the SSA domain. Some of the unique abilities of a radar system over the

traditional optical systems (e. g. [3, 4, 5]) are: independence of weather conditions, measuring the Doppler shift which allows a radial velocity estimation, and the ability to add more radar stations to form a synchronized network for enhanced performance. A Digital Array Radar (DAR) also has some advantages over a single dish antenna. One example is fast switching of the transmitter look direction through digital steering, which allows surveillance of large areas. Another one is the ability to construct various receive beams for optimal tracking and coverage. An investigation of the DAR potential in the SSA environment is brought in [6].

Several radar systems for SSA are spread globally [7, 8, 9, 10, 11]. The recently active system called the German Experimental Space Surveillance and Tracking Radar (GESTRA), holds some unique features and will be the center of this paper. Its novelty lies in being a semi-portable pulsed DAR system, designed for the surveillance of space debris.

Recently, first dozens of successful system experiments were made, targeting known LEO objects. In these *Spotlight Mode* (a. k. a. *beampark*) experiments, the radar's estimation performance of the objects were analyzed: range, radial velocity and acceleration, Direction of Arrival (DOA) and Signal-to-Noise-Ratio (SNR). In the final operational stage of the system, these parameters are used for the debris trajectory estimation.

In this contribution, an overview of GESTRA and its Signal Processing (SP) is given, along with a complete description of the experiments. Thereafter, we analyze the results and compare them with propagated Two-Line Element (TLE) data and theoretical resolution limits. Lastly, conclusions and future outlook on the various research directions are given.

2. GESTRA

Since 2014, the Fraunhofer Institute for High Frequency Physics and Radar Techniques (FHR) has been developing and building a DAR system for SSA, called GESTRA. This section describes the GESTRA system, which is a semi-portable ground based pulsed DAR system operating in L-band (1280 MHz – 1380 MHz).

While GESTRA is originally designed for quasi-monostatic or bistatic operation, it offers the capability to build multistatic networks by adding additional receiver or transmitter stations respectively. Using this network approach is very attractive, since it enables gradual performance enhancements by adding more nodes over time. The option to transport the Tx (transmission) and Rx (receiving) units allows additional flexibility in the network geometrical design. An overview of network configurations and GESTRA units is available in [12, 13].

2.1. Technical Parameters

The receiving and transmitting stations are allocated in two distinct semi-portable shelters with a distance of about 100 m. Each shelter has a size of 18 m × 4 m × 4 m and a radome with a height of 4.5 m. Fig. 1 shows both Tx and Rx parts at an operational quasi-monostatic configuration.

GESTRA comprises of two large circular antenna arrays, digital beamforming, dual Rx polarization (to mitigate atmospheric effects), 3D mechanical positioners, separated autonomous transmit and receive array sub-systems, which enables both quasi-monostatic and bistatic modes of operation.

Both Tx and Rx antenna apertures contain 256 active cavity-backed stacked patch antennas surrounded by 64 dummy elements within circular planar apertures with diameters of 3 m and identical element distribution. The two arrays are mounted on identical mechanical 3D positioners to set up the coarse Field of View (FOV) in space. The positioners allow a mechanical rotation angle of 0° to 360° in azimuth and 0° to 100° in elevation additionally to the mechanical 90° polarization rotation of the third axis.

On both the transmitter and receiver side digital beamforming is used to steer the respective beams off of the mechanical steering position. On the receiver it is possible to process up to 16 beams in parallel, to have the ability to reduce the SP computational load of 256 elements, while maintaining the ability to estimate the DOA within the desired spatial sector.

The parameters of the GESTRA system are summarized in Table 1. Since some of the values are mode-dependent (marked with *), we present their typical values.

2.2. Operation Modes

This section gives an overview of the operational modes of the GESTRA system, to allow different coverage volumes by adjusting the space fence size and system parameters (e. g. waveform, Coherent Processing Interval (CPI), etc.). They are part of an initial configuration and can be changed according to the use case. There are three

Table 1. GESTRA system typical parameters.

Parameter	Value
No. of antenna elements	256
System noise figure	< 1.5 dB
Tx output power	> 1,000 W
Tx length*	up to 8.5 ms
PRF*	30 Hz
No. of pulses* per CPI	3–24
Beamwidth*	6.5°
Max. scan area	±45°
Directivity	30.9 dB
Angular accuracy	0.6° @ 11 dB SNR
Range accuracy	75 m @ 11 dB SNR
Target range	300 km – 4,400 km
Carrier frequency*	1.33 GHz
Bandwidth	2 MHz
Steering method	Elect. and mech.

main types of modes: surveillance, tracking, and experimental.

The main goal of the surveillance modes is to guarantee a continuous observation of the targeted FOV volume, by electrical steering of the array's antennas. The idea is to steer the antenna in one direction, send a dedicated number of pulses (i. e. several CPI bursts) and then shift to the next position. One scan cycle is the procedure of switching to all necessary positions that are configured in the currently used mode. To get a continuous observation, the time used for a complete scan cycle is limited by the FOV crossing duration of the observed particles. This depends on the orbital height of the debris particle, and will have the shortest scan duration for the minimal orbit height.

The aim of the tracking mode is to observe a known debris particle as long as possible by following it with the Tx steering, and then use the data to update the orbit information. There are also two experimental modes: the first one enables receiving with dual polarization, the second mode is designed to achieve better range resolution.

3. SIGNAL PROCESSING

SSA poses many challenges for the DAR system's SP block. It requires the detection and parameter estimation of extremely far and small targets moving at incredible velocities (up to 30,000 km/h) and high radial accelerations (e. g. 200 m/s²), orbiting at altitudes between 300 km and 3,000 km.

In turn, the SP must cover a wide set of possible target ranges, radial velocities and accelerations, sizes, rotations, polarized reflections and more. Additionally, the detection of multiple targets with a large range gap, or hazardous fragmentation events, could suffer from the masking effect if a proper waveform is not applied [14, 15]. In this section we present a high level descrip-



Figure 1. Photo of the Tx and Rx sub systems at the site in Koblenz, Germany.

tion of some of the used concepts and algorithms concerning SP. We refer the reader to [6] for an in-depth DAR SP overview adapted to SSA.

3.1. Range-Doppler Compression

One central aspect in every radar's SP is the Range-Doppler (RD) compression. This crucial and computationally demanding process finds the RD values of the target, usually under linear motion migration between the pulses. As the radial velocity and acceleration can reach high values in SSA, the Doppler shift can have an impact even within a single pulse. As we show next, some modifications had to be made to adapt this stage to the SSA scenario.

The signal being transmitted can be written as a combination of a complex baseband signal $s(t)$ that is up-converted to a given carrier frequency f_c

$$\tilde{s}(t) = \text{Re} \{ s(t) e^{j2\pi f_c t} \}. \quad (1)$$

Assuming a single target at some distance $r(t)$ from the radar and no direct signal between transmitter and receiver, the received signal is a weighted and delayed (and stretched in some cases) version of the transmit signal. The down-converted, received complex baseband signal (for a single antenna element) is written as

$$y(t, \boldsymbol{\theta}) = \gamma \underbrace{s(t - \tau(t, \boldsymbol{\theta})) e^{-j2\pi f_c \tau(t, \boldsymbol{\theta})}}_{b(t, \boldsymbol{\theta})}. \quad (2)$$

The amplitude factor γ in (2) is depending on the range (representing the propagation loss), the target's Radar Cross Section (RCS), and antenna two-way gain (DOA

dependent). The vector $\boldsymbol{\theta} = [r_0, v_{r,0}, a_r]$ contains the unknown parameters related to the specific target: range, radial velocity and acceleration, respectively. The '0' subscript refers to some choice of initial time (e. g. beginning of the pulse).

Compared to other radar applications, the potential targets could be thousands of kilometers away, which both enables and requires the use of long Tx pulses, to allow higher energy transmission. The term $\tau(t)$ is the delay of the signal arriving at the receiver at time t , given by the implicit equation

$$\tau(t) = \frac{2r \left(t - \frac{\tau(t)}{2} \right)}{c_0}, \quad (3)$$

where $r(t)$ is the range at time t and c_0 is the speed of light. This equation states that the delay measured at a given time instance t is proportional to the range that the target had at $t - \tau(t)/2$.

Since the target is fast-moving in orbit, the range and delay changes over time. The time-dependent range can be approximated as the following quadratic function

$$r(t) = r_0 + v_{r,0}t + \frac{1}{2}a_r t^2. \quad (4)$$

Inserting (4) into (3) and removing negligible quadratic terms, we can solve the implicit equation in order to get

$$\tau(t) = \frac{2r_0 + 2v_{r,0}t + a_r t^2}{c_0 + v_{r,0} + a_r t}. \quad (5)$$

We now write the RD equation as

$$RD(\boldsymbol{\theta}) = \int x(t)b^*(t, \boldsymbol{\theta})dt, \quad (6)$$

where $x(t)$ is the received measured baseband signal, and $b(t, \theta)$ is used as the template signal. The unknowns in θ are estimated using a correlation (or matched-filter) based approach where the actual received data is correlated with the template signal. The set of parameters maximizing the correlator output is used as an estimate of θ . The SNR is also derived from the response magnitude and the known noise statistical distribution.

The direct time-domain calculation of (6) has a heavy computational load, which practically prevents any real-time or reasonable response time. On the other hand, the non-linearity of $\tau(t)$ in (5) prevents the use of an efficient Fast Fourier Transform (FFT) to solve (6).

A common simplification to circumvent this problem is known as the *stop-and-go* approximation, which assumes that the motion of the target during the wave's traveling time can be disregarded. Moreover, the range migration effect is often neglected due to short pulse trains and/or coarse range resolution. In addition with a zero radial acceleration assumption, $\tau(t)$ will have a linear dependency, allowing the desired use of the FFT.

However, in our scenario, these approximations cannot be made, as the target's radial velocity cannot be neglected even within the time frame of a single pulse. In addition, the radial acceleration cannot be neglected across the CPI.

To accommodate these conditions, we developed our own target response model and SP filter bank for the parameter estimation. We distinguish these into two different types: the time-delay within the argument of $s(t)$ and the phase term in the exponent from (2).

The first step assumes the radial velocity in a single pulse duration is small enough such that $s(t - \tau)$ can be used in (2). Despite using long pulses, this is still possible in the GESTRA context because of the relatively small bandwidth. We note that this cannot be applied on the phase term.

The second simplification exploits the radial velocity being (approx.) constant within a pulse. Thus, the phase term has a linear fast-time dependency. Re-writing (2) will now yield

$$y(t, \theta) = \gamma s(t - \tau(\theta)) e^{-j2\pi f_c \zeta(t, \theta)}, \quad (7)$$

where $\zeta(t)$ is a linear function of t . The FFT can now be used to solve (6) for each pulse separately, in an efficient and practical manner. In-between pulses we follow the non-linear motion in (4) without any simplification. A full description of this stage is outside the scope of this paper, and is planned to be published in a separate contribution.

3.2. Parameter Estimation

The process of estimating the parameters in θ starts with a 3D discretized search space, i. e. a set of possible pa-

rameter values $(r_0, v_{r,0}, a_r)$. This search space is upper-/lower-bounded by the procedure described in [16, 17], which reports a dependency of the possible combination of range, radial velocities and accelerations. Due to orbital dynamics, for a given range the possible radial velocities and accelerations are limited. The coupling between radial acceleration and range is particularly strong. Since the FFT permits processing multiple range values simultaneously, we divide the search space into acceleration slices (each with a constant value) that deal with different range intervals.

The integration of pulses within a CPI can be done both coherently and noncoherently. However, since a CPI can be relatively long, e. g. 0.8 seconds, a coherent approach requires a very fine grid in both $v_{r,0}$ and a_r . For the experimental processing on the average workstation, the coherent computational load is impractical. Therefore, we start with a noncoherent preprocessing using a coarse grid.

If the noncoherent estimated SNR value meets a certain predefined threshold (e. g. Neyman Pearson [18]), a detection is declared. These results are used as an initialization for a smaller search grid of the coherent case.

We note that the described processing is performed for a number of different channels, where a channel constitutes a specific beam using digital beamforming. The results for different channels can be used in a Maximum Likelihood Estimator (MLE) to estimate the DOA in a predefined spatial sector (under the condition that the same range, velocity and acceleration estimates are utilized). The angular motion of the target within one CPI should be taken into account as shown in [19] to avoid estimation bias.

At the final stage of the SP, an object's estimated location, radial velocity and acceleration (with their corresponding uncertainties), are collected for a series of time-stamps. These are delivered to the German Aerospace Center (DLR) control room, where the expected trajectory and orbit determination are calculated [20].

4. EXPERIMENT SETUP

To validate the system performance, the initial conducted experiments' goal was to detect known LEO targets and estimate several parameters: range, radial velocity and acceleration, DOA, and SNR. The test targets were selected based on publicly available TLE data, serving as both a basis for setting up the experiments as well as the ground-truth for evaluating the estimated parameters.

We analyze a specific mode called the *Spotlight Mode*. This mode is used for every radar task that demands an optimal detectivity in a dedicated direction. During the experiments the antenna array is mechanically steered in one fixed observing direction. Satellites penetrating the Tx/Rx beams are detected and the orbital parameters as range, DOA, etc. are then estimated.

Fig. 2 shows a simplified sketch of the setup. The red cone indicates the transmit beam 3-dB area, while several receive beams are placed such that the whole illuminated volume is covered. In the DOA estimation process, we use the uv directional cosine coordinate system as seen by the Rx array, which can be interpreted as a projection of the azimuth and elevation angles onto the *North-East*-plane [21].

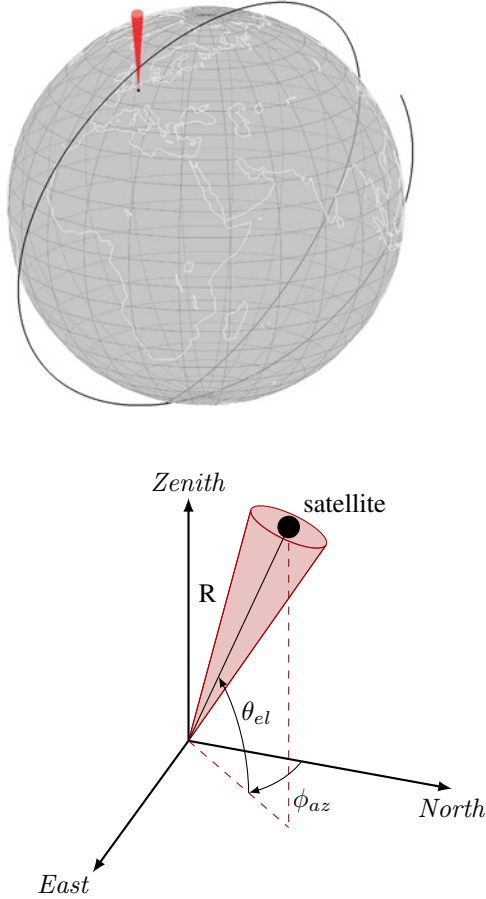


Figure 2. Satellite orbit pass through the beam (top). Definition of range, azimuth and elevation (bottom). The radar station is at the origin. The Tx beam 3-dB volume is marked by the red cone.

4.1. Target Objects

There are various objects in the LEO with different characteristics and orbit parameters that are suitable for verification of the GESTRA system. These include active/defunct satellites, Rocket Body (RB) parts and fragmentation debris from certain collision events (e.g. COSMOS-1408). When EO satellites are active, their orientation is aligned to earth's surface. However, RBs may be rotating around themselves in an uncontrolled manner. A debris cloud caused by a collision event contains a group of smaller particles moving in similar ranges and velocities.

Some 50 experiments were recently made, covering around 20 different objects. These include the TERRA, SWARM, Lincoln Calibration Sphere (LCS-4), Environmental Satellite (Envisat), SB-14-RB, COSMOS-1408-DEB, BLUEWALKER and more. Information about the orbits can be found in [22].

In this paper we focus on two objects summarized in Table 2. The LCS-4, is an aluminum sphere which is used for radar calibration. It has a constant RCS and well known orbit parameters (more data in [22, 23, 24]). One of the most popular space debris is the Envisat. It is a defunct satellite with a staggering RCS of 18.6 m^2 , which serves as a counterexample with very high SNR values. This satellite was used for EO before the contact was lost and the mission ended [25, 26]. It is now considered to be the largest space debris in orbit (see Fig. 3).

Table 2. Objects data.

Name	LCS-4	Envisat
NORAD ID	5398	27386
Type	Calibration sphere	Defunct satellite
Geometry [m]	diam. = 1.12	26 x 10 x 5
RCS [m^2]	0.95	18.6
Apogee [km]	822	765
Perigee [km]	732	764

4.2. System Configuration

The various parameters of the system for the initial experiments are presented in Table 3. For a maximum SNR and low radial velocities, each experiment duration was around one minute, centered around the expected Closest Point of Approach (CPA) with an elevation larger than 70° . Due to the preliminary stage of the tests, the duty cycle was kept below 25%. In addition, only target ranges $400 \text{ km} < r < 1000 \text{ km}$ were considered, to allow lower data volumes transfer and to ensure the waveform transmission does not overlap with reception.

Some other aspects are still undergoing validation (e.g. range and antenna elements calibration), due to the initial state of the system and the fact that only (fast-moving) space objects can be used for measurements verification.

Table 3. GESTRA system experiments parameters.

Parameter	Value
No. of antenna elements	200
No. of Rx beams	5 – 16
Tx length	2 ms – 4 ms
PRF	30 Hz – 90 Hz
No. of pulses per CPI	24
Beamwidth	6.5°
Waveform	Costas code, LFM
Bandwidth	2 MHz



Figure 3. LCS Photo (left) Envisat model photo (right). Taken from [23] and [27].

5. EXPERIMENT RESULTS

In this section the result comparison and validation methods are described. The Envisat experiment took place on the 25.10.2022 at 15:01, and the LCS-4 on the 04.11.2022 07:34 (CET time zone).

5.1. Ground Truth Data

For evaluation of the results of GESTRA, ground-truth data is needed – the TLE is used as the data source for in-orbit objects. It contains position and velocity information for a specific time-stamp and object. Usually, there is a large time gap with the experiments' time (e. g. up to several days). Therefore, the TLE closest to the time of experiment is downloaded from [28] and then propagated to the exact time-stamps of the experiment, using an implementation of a Simplified General Perturbations 4 (SGP4) propagator [29, 30]. From the propagated trajectory of the object, the range, radial velocity, radial acceleration, etc. are then derived. We note that the TLE datasets contain some uncertainties that are not published and can be a cause of mismatch between observed/estimated and propagated parameters.

In addition, there is a difficulty in determining the true RCS and subsequently the SNR for the majority of the objects. For some objects an RCS value can be found (see [22]) while for other it is either unknown or classified. However, even for existing RCS values, only the average value is reported, while the instantaneous value depends on aspect angle and wavelength of the illumination signal. One special case is the LCS-4 which being a sphere has a constant RCS irrespective of its orientation.

Another important task is the detection assignment resulting from the SP to a specific cataloged object. For that purpose, all possible objects in a given time-stamp

are tested for proximity to the estimated parameters. The one with the closest values is chosen. A final stage of outlier removal is then performed – if the associated TLE propagated values are too far from the estimated ones, the detection is declared to have no TLE counterpart and removed from the analysis.

5.2. Parameter Estimation Analysis

Since the targets were all pre-known, there was no SNR threshold to declare a detection, and false alarm was not an issue. Thus, a single target was assumed at all times, and the response with maximum SNR was always chosen from all acceleration partitions and all channels.

The in-depth parameter estimation is presented in Fig. 4. We see the expected parabolic range behavior as a function of time (in CPI units), as the object comes and goes, while the velocity remains linear and symmetric around the CPA. As assumed in the SP scheme, the radial acceleration remains constant within one CPI, and slowly changes across the experiment.

The estimated range curve overlaps with the propagated TLE one, where only a small bias in the y-axis is present. A bias in the x-axis would point to a timing problem, caused either by the system or the TLE.

The expected SNR given by the TLE is derived using an approximated constant RCS value, using the system parameters from Table 3 in the range equation formula [31]. We can see the SNR has a good match around the CPA, with increasing difference as the object leaves the main Tx beam area. Outside this area, it is possible that slight Tx/Rx pattern inhomogeneities occurs that do not fit the original design. Due to a much stronger SNR, the Envisat estimations are with higher accuracy.

The difference in SNR between coherent and non-

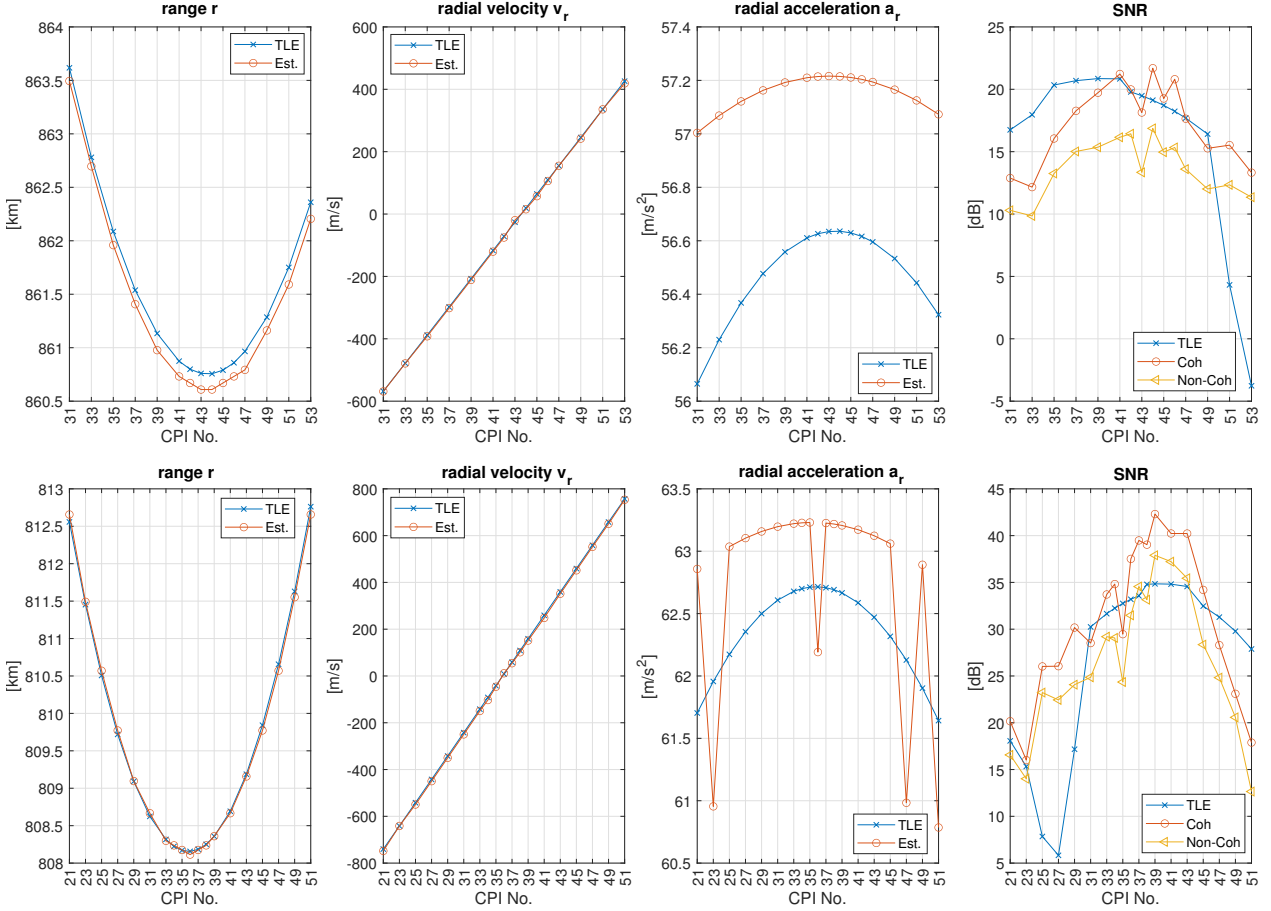


Figure 4. Parameter estimation of object LCS-4 (top) and Envisat (bottom). Each CPI duration is 0.8 seconds. Good result overlap is observed, with errors smaller than 61 m in range and 10 m/s in radial velocity.

coherent integration is clearly shown and matches the expected values. As the number of pulses increases, the coherent method will be more advantageous (with a higher cost in computation time). Due to the reason brought in Sect. 5.1 regarding RCS values, we note that the comparison of SNR should be treated with care.

Fig. 5 shows the estimation results of the DOA for Envisat. The findings are plotted in a combined uv diagram with the object passing from "right-to-left", i. e. the earlier CPIs can be found at positive u -values while the trajectory goes towards negative u -values. It can be seen that the object's DOA is followed nicely by the estimation scheme. The absolute errors are on average smaller than 0.0094 in u and 0.0013 in v , which translates into azimuth error smaller than 1.67° and 0.10° in elevation. Due to the proximity to zenith, the azimuth becomes degenerate. Hence the slightly larger azimuth error is both expected and tolerated.

In addition to the DOA the plot also depicts the layout of the 16 receive beams' 3-dB curves as green circles. Each Rx beam (numbered from 1 to 16) covers a different spatial sector, with some overlap to its neighboring beams.

The experiment was designed so the CPA will occur close to the center of the Rx beams pattern (i. e. beam number 9). The DOA estimation was performed using the entirety of all 16 beams. We note that other beam configurations for the SSA scenario are available in [32].

The parameter estimation is performed using a 3D grid based search. The grid spacing in the coherent processing case in range is approx. 61 m and 0.07 m/s in radial velocity. These values are based on theoretical considerations from [33]. The radial acceleration theoretical limit is around 0.1 m/s^2 . Due to the high computational load of such a finer grid, the spacing was set to 1 m/s^2 .

We see that the mean error in range is optimal, as it reaches the grid spacing and theoretical limit. The radial velocity accuracy, however, does not always reach the spacing. The radial acceleration error reaches the spacing, but may cause some straddle loss. It must be noted that the different parameters cannot be treated independently but they influence each other. This means e. g. that an error in the estimated radial acceleration also influences the quality of the other estimates. The exact choice of the optimal (i. e. smallest) grid size in all three param-

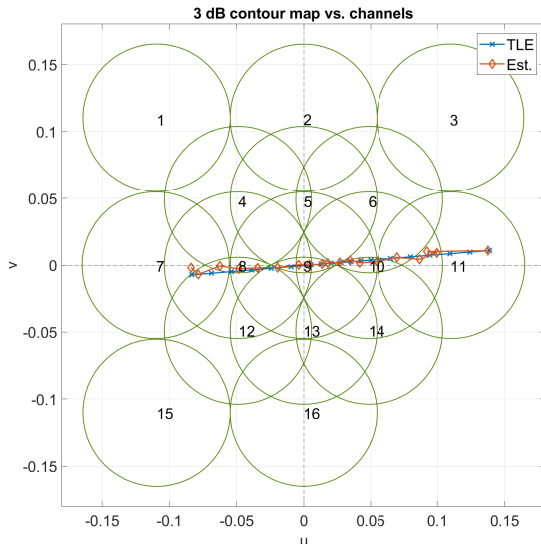


Figure 5. Estimated DOA of Envisat in uv -coordinates. Rx beams 3-dB contours are marked in green, for each channel number. Each marker represents a different CPI.

eter dimensions is still subject to further analysis, as well as the computation of the Cramér-Rao-Bound (CRB) as a lower bound on the expected estimation error variances.

The mean localization (position) error for these experiments is around 5 km – 7 km. This error is the absolute distance between the estimated location in space, and the one provided by the TLE propagation. The position calculation uses the range and DOA estimations. Due to the far ranges of the targets, the localization accuracy is very sensitive to the DOA estimation quality – every fraction of a degree offset causes kilometers of localization error. While only two experiments are analyzed here, these performances were similar throughout the majority of the experiments mentioned in Sec. 4.1.

6. CONCLUSIONS

While GESTRA is still in its initial test phases, preliminary results show great promise. The new RD compression method proved to be fast and accurate, without the need for the conventional *stop-and-go* or zero acceleration assumption. Both small and large LEO objects were accurately estimated (reaching the system’s specifications) in the *Spotlight Mode*, which makes a good start for other operational modes. Additional work on the DOA accuracy and antenna elements calibration will further improve the localization accuracy.

Future work includes the detection of space fragmentation events and debris cloud, which poses a great threat to Earth’s space infrastructure. Fast rotating objects (e. g. tumbling RBs) are currently undergoing experiments. Additional Rx beam patterns, Tx waveforms and detec-

tion methods will be studied as well. Lastly, the creation of a GESTRA network holds the key for enhanced performance, and is currently under intensive research in the FHR institute with future projects already underway.

ACKNOWLEDGMENTS

For the successful build-up of the system, we point out the exceptional work done by the other parts of the GESTRA project team. Especially, for the large number of experiments performed by Mr. Olaf Peters.

The work presented in this paper was performed on behalf of the German Space Agency with funds of the German Federal Ministry of Economic Affairs and Technology under the grant No. 50LZ1401.

REFERENCES

1. NASA. Space debris. https://www.nasa.gov/centers/hq/library/find/bibliographies/space_debris. [Accessed 19/01/2023].
2. J. Amos. International Space Station in debris scare. *BBC*, 2011.
3. R. Swindle, D. Hope, M. Hart, and S. Jefferies. High-resolution space situational awareness imaging using carbon fiber telescopes. *Journal of Applied Remote Sensing*, 12(4), 2018.
4. R. Musci, T. Schildknecht, and M. Ploner. Orbit improvement for GEO objects using follow-up observations. *Advances in Space Research*, 34(5):912–916, January 2004.
5. T. Schildknecht, R. Musci, M. Ploner, G. Beutler, W. Flury, J. Kuusela, J. de Leon Cruz, and L. de Fatima Dominguez Palmero. Optical observations of space debris in GEO and in highly-eccentric orbits. *Advances in Space Research*, 34(5):901–911, January 2004.
6. N. Neuberger. *Signal Processing for Space Surveillance Radar*. PhD thesis, Siegen University, February 2022.
7. L. N. Johnson. U.S. Space surveillance. *Advances in space research*, 13(8):5–20, 1993.
8. G. Fonder, M. Hughes, M. Dickson, M. Schoenfeld, and J. Gardner. Space fence radar overview. In *2019 International Applied Computational Electromagnetics Society Symposium (ACES)*, 2019.
9. T. Michal, J. P. Eglizeaud, and J. Bouchard. Graves: the new french system for space surveillance. In *Proceedings of the 4th European Conference on Space Debris (ESA SP-587)*, pages 61–66, April 2005.
10. J. Ender, L. Leushacke, A. Brenner, and H. Wilden. Radar techniques for space situational awareness. In *2011 12th International Radar Symposium (IRS)*, pages 21–26, 2011.

11. J. Rowland, D. McKnight, B. Prado Pino, B. Reihs, and M. A. Stevenson. A worldwide network of radars for space domain awareness in low earth orbit. In *2021 Advanced Maui Optical and Space Surveillance Technologies Conference (AMOS)*, 2021.
12. R. Hoffmann, S. Jonkers, R. Kohlleppele, A. Charlish, and H. Schily. Performance evaluation of a distributed radar system for space surveillance. In *2019 IEEE Radar Conference (RadarConf)*, April 2019.
13. R. Hoffmann, N. Neuberger, and R. Vehmas. Rx beamforming for long baseline multistatic radar networks. In *2021 IEEE Radar Conference (RadarConf21)*, pages 1–6, 2021.
14. N. Neuberger and R. Vehmas. A Costas-based waveform for local range-Doppler sidelobe level reduction. *IEEE Signal Processing Letters*, 28:673–677, 2021.
15. N. Neuberger and R. Vehmas. Range sidelobe level reduction with a train of diverse LFM pulses. *IEEE Transactions on Aerospace and Electronic Systems*, 58(2):1480–1486, 2022.
16. R. Kohlleppele. Extent of observation parameters in space surveillance by radar. In *2018 19th International Radar Symposium (IRS)*, pages 1–7, 2018.
17. H. Wilden, N. Ben Bekhti, R. Hoffmann, C. Kirchner, R. Kohlleppele, C. Reising, A. Brenner, and T. Eversberg. GESTRA - recent progress, mode design and signal processing. In *2019 IEEE International Symposium on Phased Array System & Technology (PAST)*, pages 1–8, 2019.
18. S. M. Kay. *Fundamentals of Statistical Signal Processing: Estimation Theory*, volume 1. Prentice Hall PTR, 1993.
19. N. Neuberger and R. Vehmas. On maximum likelihood DoA estimation for space surveillance radar. In *2021 29th European Signal Processing Conference (EUSIPCO)*, pages 1880–1884, 2021.
20. D. A. Vallado. *Fundamentals of Astrodynamics and Applications*. Microcosm Press, 4th edition, 2013.
21. H. L. Van Trees. *Optimum array processing: Part IV of Detection, Estimation, and Modulation theory*. John Wiley & Sons, 2002.
22. T. S. Kelso. Satellite catalog SATCAT. <https://celestrak.org/satcat/search.php>. [Accessed 13/01/2023].
23. G. D. Krebs. “LCS 1, 2, 3, 4”. Gunter’s space page. https://space.skyrocket.de/doc_sdat/lcs-1.htm. [Accessed 13/01/2023].
24. J. Louet. The Envisat mission and system. https://www.esa.int/esapub/bulletin/bullet106/bull106_1.pdf, June 2001.
25. European Space Agency (ESA). ESA declares end of mission for Envisat. https://www.esa.int/Applications/Observing_the_Earth/Envisat/ESA_declares_end_of_mission_for_Envisat, May 2012.
26. ESA. Envisat. <https://earth.esa.int/eogateway/missions/envisat>. [Accessed 19/01/2023].
27. Wikipedia. Envisat. <https://en.wikipedia.org/wiki/Envisat>. [Accessed 19/01/2023].
28. SAIC. space-track.org. <https://www.space-track.org>. [Accessed 12/01/2023].
29. D. A. Vallado and T. S. Kelso. Astrodynamics software. <https://celestrak.org/software/vallado-sw.php>. [Accessed 19/01/2023].
30. D. A. Vallado, P. Crawford, R. Hujsak, and T. S. Kelso. Revisiting spacetrack report 3: Rev 3. In *AIAA/AAS Astrodynamics Specialist Conference and Exhibit*, page 6753, 2006.
31. M. A. Richards, J. A. Scheer, and W. A. Holm. *Principles of Modern Radar*. SciTech Publishing Inc, 2010.
32. N. Neuberger, R. Vehmas, and J. H. G. Ender. Dimension-reduced Rx beamforming optimized for simultaneous detection and estimation. *IEEE Transactions on Aerospace and Electronic Systems*, 57(4):2501–2513, 2021.
33. D. K. Barton. *Radar System Analysis and Modeling*. Artech House radar library. Artech House, 2005.